STRAIN-ACTUATED SOLAR ARRAYS FOR SPACECRAFT ATTITUDE CONTROL ASSISTED BY VISCOELASTIC DAMPING

Yong Hoon Lee[1]*, Vedant[2], Randy H. Ewoldt[1], James T. Allison[2,3]

[1]*Dept. of Mechanical Science and Engineering, University of Illinois at Urbana-Champaign, Urbana, IL 61801, USA*
** Corresponding author: ylee196@illinois.edu*
[2]*Dept. of Aerospace Engineering, University of Illinois at Urbana-Champaign, Urbana, IL 61801, USA*
[3]*Dept. of Industrial and Enterprise Systems Engineering, University of Illinois at Urbana-Champaign, Urbana, IL 61801, USA*

Abstract

This article presents a utilization of viscoelastic damping to reduce control system complexity for strain-actuated solar array (SASA) based spacecraft attitude control systems (ACSs). SASA utilizes intelligent structures for attitude control, and is a promising next-generation spacecraft ACS technology with the potential to achieve unprecedented levels of pointing accuracy and jitter reduction during key scientific observation periods. The current state-of-the-art SASA implementation utilizes piecewise modeling of distributed piezoelectric (PZT) actuators, resulting in a monolithic structure with the potential for enhanced ACS reliability. PZT actuators can operate at high frequencies, which enables active vibration damping to achieve ultra-quiet operation for sensitive instruments. Relying on active damping alone, however, requires significant control system complexity, which has so far limited adoption of intelligent structures in spacecraft control systems. Here we seek to understand how to modify passive system design in strategic ways to reduce control system complexity while maintaining high performance. An integrated physical and control system design (co-design) optimization strategy is employed to ensure system-optimal performance, and to help understand design coupling between passive physical aspects of design and active control system design. In this study, we present the possibility of utilizing viscoelastic material distributed throughout the SASA substructure to provide tailored passive damping, intending to reduce control system complexity. At this early phase of study, the effect of temperature variation on material behavior is not considered; the study focuses instead on the design coupling between distributed material and control systems. The spatially-distributed design of both elastic and viscoelastic material in the SASA substructure is considered in an integrated manner. An approximate model is used that balances predictive accuracy and computational efficiency. This model approximates the distributed compliant SASA structure using a series of rigid links connected by generalized torsional springs and dampers. This multi-link pseudo-rigid-body dynamic model (PRBDM) with lumped viscoelastic damping models is derived, and is used in numerical co-design studies to quantify the tradeoffs and benefits of using distributed passive damping to reduce the complexity of SASA control systems.

Keywords: *Spacecraft attitude control system, Strain-actuated solar array, Viscoelastic damping, Co-design*

1. Introduction

After the success of the Hubble and other space telescopes, goals for next-generation space observatories, such as the James Webb space telescope, demand higher pointing precision [1], enabling discoveries such as finding the first luminous sources and reionization histories from the early universe. Angular orientation of current spacecraft, including state-of-the-art space observatories, is controlled by reaction control system (RCS) thrusters, momentum exchange devices including reaction wheel actuators (RWA), and other devices [1,2]. These conventional attitude control systems (ACS), however, often make unwanted disturbances (jitter) that hinder precise pointing for clear and noise-free deep space observation [3]. Recent studies suggest that small slewing maneuvers, precision pointing, and jitter suppression can be simultaneously achieved by using strain-actuated solar arrays (SASAs), a novel ACS based on intelligent structures [4,5]. The SASA architecture proposed earlier includes piezoelectric (PZT) strain actuators bonded to solar panel surfaces and/or on the panel-to-panel vane for a small-angle control, and a solar array (SA) root actuator for larger slewing motion [4]. One drawback of the SASA architecture is that the control system for the root actuators and strain actuators needs to handle all vibration frequencies actively via PZTs, which demands a high-frequency, sophisticated control system. A

possible remedy is to add strategic passive damping to the SASA system to manage high-frequency vibration modes. Active control can then focus more on low-frequency dynamics, with possibly more aggressive control laws than without tailored passive damping. An initial effort introduced a conceptual viscoelastic damping system to reduce ACS system complexity by passively diminishing vibrations [6]. The model developed for this previous work included a full two-dimensional (2D) spacecraft model with two single-joint solar panels using a single revolute-joint pseudo-rigid-body dynamic model (1R-PRBDM). An improvement in peak vibration amplitude reduction was observed, but adding viscoelastic material did not improve overall system performance (maximum slew angle). This may have been due to omission of *material functions* (i.e., function-valued material properties) as design variables in the study, and a performance improvement is expected by exploring the optimal material function parameters [7].

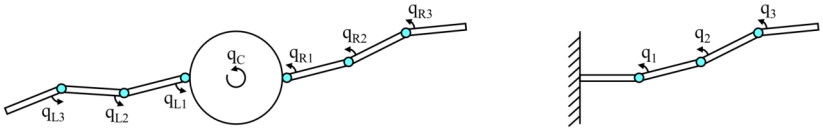

(a) Conceptual SASA system model (b) SASA system unit test model

Figure 1. PRBDM configurations of conceptual SASA system and its unit test models

In this study, we expand on previous work by investigating SASA with viscoelastic damping involving: (1) a multiple revolute-joint pseudo-rigid-body dynamic model (nR-PRBDM) [8], (2) a unit test model of the SASA system, (3) design of the viscoelastic material function, and (4) more realistic modeling of a revolute-joint damping component using a 2D axisymmetric shear flow model. The design problem we propose in this study contains torque control trajectories at each revolute joint and viscoelastic fluid material function parameters as design variables. A simultaneous material and control optimization formulation is used, based on a specific spacecraft maneuver. Figure 1(a) illustrates the nR-PRBDM SASA modeling concept. Total system momentum must be conserved in this configuration; SASA controls spacecraft attitude via momentum transfer. As a simplification for this study, the rigid-body mode is eliminated, as illustrated in Figure 1(b). This still supports study of the movement of a multi-body system with active control and viscoelastic passive damping. Reference [6] details the full spacecraft PRBDM shown in Figure 1(a), which is outside the scope of this article.

2. Methods

2.1 Viscoelastic Damper Model

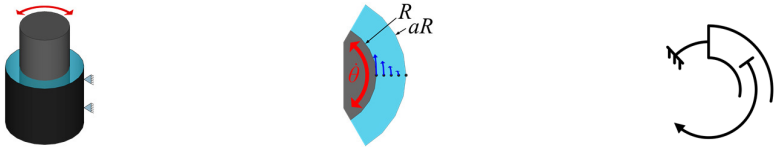

(a) 2D axisymmetric model (b) Mesh points for 2D model (c) Reduced-order model

Figure 2. Schematic and implementation of viscoelastic damper models.

For the 2D axisymmetric model, we assume that the revolute joints shown in Figure 1 are concentric cylinders with viscoelastic fluid in the gap, as shown in Figure 2(a). By setting the frame of reference attached to the outer cylinder, net angular joint motion is defined as the rotation of the inner cylinder relative to the rotation of the outer cylinder. We assume that the outer cylinder is attached to the panel member closer to the spacecraft body, while the inner cylinder is attached to the panel member located farther from the center. Figure 2(b) shows a top view of the concentric cylinders and a uniformly distributed numerical mesh nodes inside the viscoelastic fluid region. For the 1D reduced-order model, we do not compute the fluid shear inside the gap, but assuming a one-dimensional (1D) translational viscoelastic dashpot in the rotational direction, as depicted in Figure 2(c).

2.1.1 Two-Dimensional Axisymmetric Model

The 2D axisymmetric model in a cylindrical coordinate was derived based on the three-dimensional (3D) Cauchy momentum equations [9]. Assuming 2D axisymmetry and linear viscoelasticity, the following assumptions are made: $u_r = u_z = 0$, $\partial/\partial\theta = \partial/\partial z = 0$, $\tau_{rr} = \tau_{\theta\theta} = \tau_{zz} = \tau_{rz} = \tau_{\theta z} = 0$, and $g_r = g_\theta = g_z = 0$. The original form of the 3D

Cauchy momentum equations is given in Eqns. (1)-(3):

$$\frac{\partial u_r}{\partial t}+u_r\frac{\partial u_r}{\partial r}+\frac{u_\theta}{r}\frac{\partial u_r}{\partial \theta}-\frac{u_\theta^2}{r}+u_z\frac{\partial u_r}{\partial z}=-\frac{1}{\rho}\frac{\partial p}{\partial r}+\frac{1}{r\rho}\frac{\partial\left(r\tau_{rr}\right)}{\partial r}+\frac{1}{r\rho}\frac{\partial \tau_{\theta r}}{\partial \theta}+\frac{1}{\rho}\frac{\partial \tau_{zr}}{\partial z}-\frac{\tau_{\theta\theta}}{r\rho}+g_r \tag{1}$$

$$\frac{\partial u_\theta}{\partial t}+u_r\frac{\partial u_\theta}{\partial r}+\frac{u_\theta}{r}\frac{\partial u_\theta}{\partial \theta}+u_z\frac{\partial u_\theta}{\partial z}+\frac{u_r u_\theta}{r}=-\frac{1}{r\rho}\frac{\partial p}{\partial \theta}+\frac{1}{r\rho}\frac{\partial \tau_{\theta\theta}}{\partial \theta}+\frac{1}{r^2\rho}\frac{\partial\left(r^2\tau_{r\theta}\right)}{\partial r}+\frac{1}{\rho}\frac{\partial \tau_{z\theta}}{\partial z}+g_\theta \tag{2}$$

$$\frac{\partial u_z}{\partial t}+u_r\frac{\partial u_z}{\partial r}+\frac{u_\theta}{r}\frac{\partial u_z}{\partial \theta}+u_z\frac{\partial u_z}{\partial z}=-\frac{1}{\rho}\frac{\partial p}{\partial z}+\frac{1}{\rho}\frac{\partial \tau_{zz}}{\partial z}+\frac{1}{r\rho}\frac{\partial \tau_{\theta z}}{\partial \theta}+\frac{1}{r\rho}\frac{\partial\left(r\tau_{rz}\right)}{\partial r}+g_z. \tag{3}$$

The governing equations given in Eqns. (4)-(5) are obtained by applying the above assumptions. This rotational shear flow is driven solely by shear stress acting in the θ-direction on surfaces with a normal in the r-direction and not by the pressure gradient; thus, Eqn. (4) represents the resultant r-direction pressure gradient and does not affect the flow. Consequently, we can use Eqn. (5) as the flow governing equation for the 2D axisymmetric model.

$$\frac{u_\theta^2}{r}=\frac{1}{\rho}\frac{\partial p}{\partial r} \tag{4}$$

$$\frac{\partial u_\theta}{\partial t}=\frac{1}{r^2\rho}\frac{\partial\left(r^2\tau_{r\theta}\right)}{\partial r}=\frac{1}{r^2\rho}\left(2r\tau_{r\theta}+r^2\frac{\partial \tau_{r\theta}}{\partial r}\right). \tag{5}$$

The linear viscoelasticity assumption does not involve normal stress behavior. Thus, from the shear stress tensor, the term in the θ-direction with respect to the r-direction only remains non-zero. The constitutive equation for the shear stress term in Eqn. (5) is:

$$\tau_{r\theta}(t)=\tau_{\theta r}(t)=\int_{-\infty}^{t}G(t-t')\gamma_{r\theta}(t')dt', \tag{6}$$

and if we assume that the system is stationary and the viscoelastic fluid has fully relaxed before the time horizon of interest, we can eliminate the integration before the time $t=0$, making the interval of the integration $(0,t)$ instead of $(-\infty,t)$. Also, the stress relaxation kernel $G(t-t')$ diminishes very quickly, being negligible after some finite time $(t-t')>t^+$. That is, the integral is approximated as zero for $t'<(t-t^+)$, giving the approximation:

$$\int_0^t G(t-t')\gamma_{r\theta}(t')dt'\approx\int_{t-t^+}^{t}G(t-t')\gamma_{r\theta}(t')dt', \tag{7}$$

where t^+ is determined by the smallest value that satisfies $G(t^+)\approx 0$ with a small tolerance. We use the single-mode Maxwell model for the kernel function, $G(t)=G_0\exp(-t/\lambda_0)$, for simplicity. The relevant shear rate component in the cylindrical coordinate system is defined as:

$$\gamma_{r\theta}=\gamma_{\theta r}=\frac{\partial u_\theta}{\partial r}-\frac{u_\theta}{r}. \tag{8}$$

where u_θ is defined within $R\le r\le aR$, a is the ratio of the radii of the outer to the inner cylinders, R is the radius of the inner cylinder, and values of these parameters are $a=1.25$ and $R=0.008$ m.

2.1.2 One-Dimensional Reduced-Order Model

The reduced-order model with a 1D translational viscoelastic dashpot in the rotational direction (Figure 1(c)) does not require a shear flow computation. The motion of the revolute joint can be approximated using a translational movement at the radius of middle-plane between the inner and outer cylinders. The constitutive equation for the shear stress is used directly for computing torque in the SASA dynamic model:

$$\tau_{r\theta}(t)=\tau_{\theta r}(t)=\int_{-\infty}^{t}G(t-t')\left[\frac{a+1}{2}R\theta(t')\right]dt'\approx\frac{a+1}{2}R\left[G(t)\theta(0)+\int_{t-t^+}^{t}G(t-t')\theta(t')dt'\right]. \tag{9}$$

The shear stress computed using Eqns. (6) or (9) is used directly in the viscoelastic torque input $T_v=\alpha_T\tau_{r\theta}$ for system dynamics prediction, where α_T is a lumped parameter that carries the geometric information of the joint, defined as:

$$\alpha_T\equiv 2\pi(aR)^2H=1.2566\times10^{-4}\ \text{m}^3 \tag{10}$$

where H is the height of the joint geometry, and the values of these parameters are set to: $a=1.25$, $R=0.008$ m, and $H=0.2$ m. Similarly, the relationship between angular displacement (or angular velocity) and shear (or shear rate), $\theta=\alpha_\theta\gamma$, $\theta=\alpha_\theta\gamma$, can be described using a lumped parameter α_θ, which is defined as:

$$\alpha_\theta \equiv \frac{2}{R(a+1)} = 1.1111\times10^{2}. \tag{11}$$

2.2 Multiple Revolute-Joint Pseudo-Rigid-Body Dynamic Model (nR-PRBDM)

This model (developed and presented in Ref. [8]) was derived to approximate compliant mechanism dynamics for use in design optimization studies, and validated for several beam configurations using finite element results. Here this model is used for design studies with both active torques and those exerted by the passive viscoelastic damper.

2.3 Design Problem Formulation

The control problem is defined within a finite time horizon with an initial position of the SASA panel and a specified final target position and velocity. The design optimization problem considered here is given in Eqn. (12):

$$\begin{aligned}
&\underset{\mathbf{x}=\left[G_0,\lambda_0,T_1,\ \ ,T_n\right]^{\mathrm{T}}}{\text{minimize}} && f=\sum_{i=1}^{n}\frac{1}{t_f-t_0}\int_{t_0}^{t_f}T_{c,i}\left(t\right)^2\,dt && \text{// obj. func.}\\
&\text{subject to} && \left(0.9\theta_1^{t_0}-\theta_1^{t_f}\right)^2=0,\ \left(0.5\theta_2^{t_0}-\theta_2^{t_f}\right)^2=0,\ \left(0.5\theta_3^{t_0}-\theta_3^{t_f}\right)^2=0,\ \left(\theta^{t_f}-0\right)^2=0 && \text{// BCs}\\
&\text{where} && \theta^{t_0}=0.2\ \text{[rad]},\ \dot{\theta}^{t_0}=0\ \text{[rad/s]}, && \text{// states ICs}\\
& && \begin{bmatrix}\theta^{k+1}\\ \dot{\theta}^{k+1}\end{bmatrix}=\begin{bmatrix}\theta^{k}\\ \dot{\theta}^{k}\end{bmatrix}+\left(t^{k+1}-t^{k}\right)\begin{bmatrix}\dot{\theta}^{k}\\ \ddot{\theta}^{k}\end{bmatrix} && \text{// time-marching}\\
& && M\left(\theta\right)\ddot{\theta}+C\left(\theta,\dot{\theta}\right)\dot{\theta}+B\dot{\theta}+K\theta-T_v\left(\tau_{r\theta}\big|_{r=R}\right)-T_c=0, && \text{// dynamics}
\end{aligned} \tag{12}$$

where a symbol with an overhead arrow represents a vector of discrete time points (e.g., $\vec{T}_1=[T_1^{k=0},T_1^{k=1},\ \ ,T_1^{k=n_k}]$), and a symbol with an arrow below is a vector of n-joints (e.g., $\underset{\rightarrow}{\theta}=[\theta_1,\theta_2,\ \ ,\theta_n]$). The objective function is a sum of integrals of squared control torque, which is a proxy of control effort from an energy perspective. Other possible objectives include maximizing slew angles in a given time period, or minimizing time required to achieve specific slew motion. The equality constraints define the boundary conditions on position and velocity at the final time, t_f. Future modeling may also include acceleration at the final time as another constraint to avoid further oscillation of the system after the final time. Initial conditions at the time t_0 are specified. The Euler forward method is used for integration within a single-shooting solution strategy. The dynamics equation is provided in a second-order differential equation form with a torque term exerted by the viscoelastic damper, T_v, and another torque term that represents the active torque control input, T_c. Note that M is the mass matrix at a certain angular pose θ; C is the Coriolis effect matrix; B is the frictional loss term (zero here); K is the stiffness matrix that quantifies passive linear torsional springs at each revolute joint.

3. Results

Figure 3(a) shows the optimal material functions for the 2D axisymmetric and 1D reduced-order model cases with a maximum control torque constraint of 10 N-m. The dotted line denotes stress relaxation modulus and the red square denotes Maxwell parameters of optimal material functions for the 2D axisymmetric case. The solid line and the black circle correspond to those material characteristics for the 1D reduced-order model case. Figure 3(b) shows the corresponding optimal control torque trajectories. Control torque trajectories are represented using a piecewise cubic Hermite interpolating polynomial with 20 equally-distributed mesh nodes.

3.1 Two-Dimensional Axisymmetric Model Design Results

Optimal Maxwell model parameters are $G_0^*=0.943$ MPa and $\lambda_0^*=1.36\times10^{-3}$ s. Displacement trajectories shown in Figure 4 are smooth and satisfy the final time boundary condition with a maximum constraint violation of 6.486×10^{-8}. Total computational time was 242 minutes for 3,186 function evaluations with a dual 2.1GHz Xeon Gold 6130 (32-core, 64-thread) workstation with the MATLAB interior-point nonlinear programming algorithm. We anticipate these results to be close to planned experimental data due to the fairly realistic model. The optimal control design exhibits some higher-frequency oscillations to mitigate vibrations due to viscoelastic material memory effects. Although viscoelastic materials can absorb a wide-range of vibration frequencies, a comprehensive evaluation of their value for SASA is not yet complete. A rigorous comparison between viscous and viscoelastic dampers will be required for determining the right choice for

this type of system. In addition, more flexible viscoelastic models may support broader design exploration and enhanced system performance.

3.2 One-Dimensional Reduced-Order Model Design Results

The Maxwell model parameters are $G_0^* = 1.09$ MPa and $\lambda_0^* = 8.69\times10^{-4}$ s, corresponding to larger initial stress and smaller relaxation time compared to the 2D axisymmetric model results. Control trajectories do resemble those from the 2D model study, but with less pronounced oscillations. Displacement trajectories satisfy the final time boundary condition with a maximum constraint violation of 1.033×10^{-10}. Total computational time was 13 minutes for 8,375 function evaluations (same hardware as before). This reduction in computational expense would enable more extensive design studies, such as a longer time horizons for multi-stage maneuvers. While control trajectories are sufficiently close to inform later design activities, the difference between Maxwell model parameters is not small, corresponding to distinct materials. One possible reason for this gap is that the 2D model accounts for transient shear flow behavior (inertia of the viscoelastic fluid), and the 1D model does not. Another possible source of disparity is the conversion of the rotational shear movement to simple translational movement. This simplification is not physically rigorous, and may require additional tuning parameters to simulate the complex shear flow behavior without solving actual shear flow mechanics.

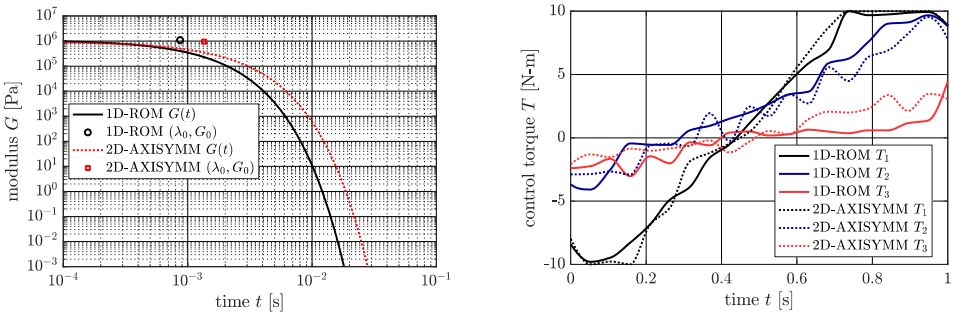

(a) Material function design (b) Corresponding control torque design

Figure 3. Optimal designs for the 2D axisymmetric and 1D reduced-order models (Maximum control torque: 10 N-m)

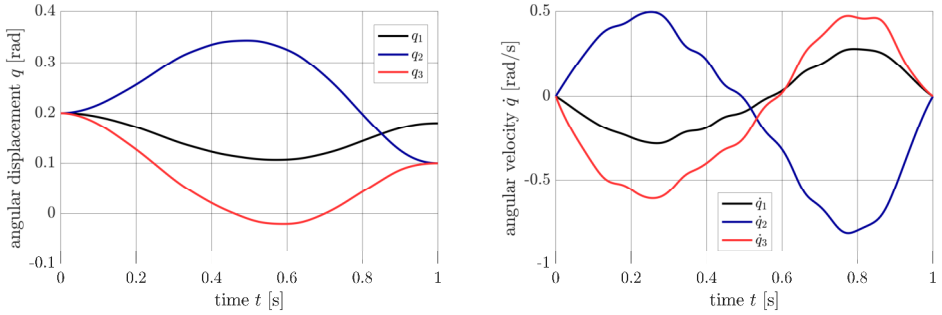

(a) Angular displacement trajectories (b) Angular velocity trajectories

Figure 4. Dynamics of the system resulting from optimal design based on the 2D axisymmetric model

3.3 Discussions on Limiting Maximum Amplitude of the Active Control System

Figure *5*(a) shows the optimal material functions for the 2D axisymmetric and 1D reduced-order model cases with varying maximum control torque constraints from 8 to 20 N-m, and Figure *5*(b) shows the corresponding optimal control torque trajectories. The case with the 20 N-m constraint does not limit the control torque, and cases with a constraint of 11 N-m and above limit the active control system very loosely. However, maximum control torque values of 10, 9, and 8 N-m cases influence the control trajectory significantly. From the material functions plot, we observe that optimal fluid design moves to higher stress relaxation time and amplitude when the control torque design space is significantly limited. Also, we observe from the trend of the optimal control torque trajectories that active control burden is distributed to multiple revolute joints when maximum capability of active control amplitude is limited. As we see from the blue colored lines in Figure *5*(b), limited control at one revolute joint (RJ) can be compensated for by having more aggressive control at the other RJs.

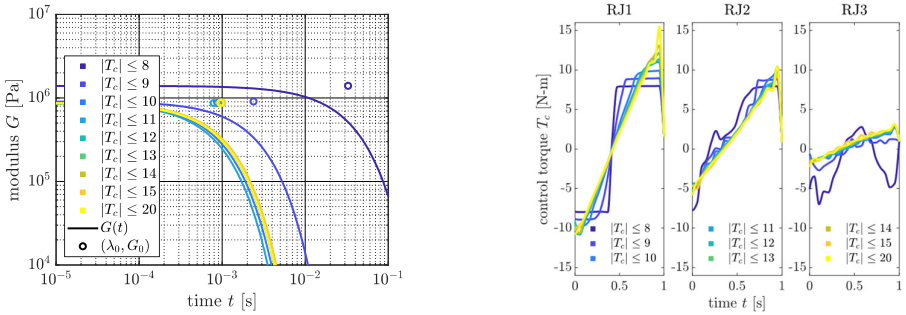

(a) Material function design (b) Corresponding control torque design

Figure 5. Optimal designs based on the 1D reduced-order models with varying maximum control torque constraints

3.4 Discussions on Vibration Frequencies

The period of the natural frequencies of the system ranges from 1.78 to 30.3 s (order of 10^0 - 10^1 s) and the control torque input is exciting the system with periods on the order of 10^{-2} s . These are at least one or more orders of magnitude larger than the characteristic relaxation time of the optimal viscoelastic fluid ($\sim 10^{-3}$ s). The optimal viscoelasticity is clearly that of a fluid with a short relaxation time compared to dominant timescales in the system dynamics, though the specific relationships between these timescales are not yet clear. Our future work with purely Newtonian fluids and viscoelastic fluids with different relaxation time ranges will study this in more depth.

4. Conclusion

The use of viscoelastic damping in intelligent structures, such as SASA, was studied here from an integrated design optimization perspective. These studies were performed using both a higher fidelity model (2D axisymmetric, transient shear flow) and a simplified model (1D reduced-order model). The latter significantly reduces computational cost, and results show similar system dynamics. Additional tuning parameters, however, may be needed to improve optimal material property identification. Viscoelasticity may help mitigate a wide range of vibration frequencies, but design effort may be costly. Future work will investigate the potential benefits of incorporating viscoelastic elements into SASA systems, and whether the additional design effort is worth the performance improvement.

Acknowledgments

This material is based upon work supported by the National Science Foundation under Grant No. CMMI-1653118.

References

1. Gardner J B, Mather J C, Clampin M, Doyon R, Greenhouse M A, Hammel H B, et al. The James Webb Space Telescope. Space Sci. Rev., 2006, 123(4): 485-606.
2. Wertz J R, editor. Spacecraft Attitude Determination and Control. Dordrecht: Springer, 1978.
3. Agrawal B. Jitter control for imaging spacecraft. In IEEE 2009 4th Int'l Conf. on RAST, 2009, Istanbul, 615-620.
4. Alvarez-Salazar O, Aldrich J, Filipe N, Allison J T, and Chung SJ. Strain actuated solar-arrays for precision pointing of spacecraft. In AAS GN&C Conf., 2016, San Diego.
5. Chilan C M, Herber D R, Nakka Y K, Chung SJ, Allison J T, Aldrich J B, et al. Co-design of strain-actuated solar arrays for spacecraft precision pointing and jitter reduction. AIAA J., 2017, 55(9): 3180-3195.
6. Lin C, Herber D R, Vedant, Lee YH, Ghosh A, Ewoldt R H, et al. Attitude control system complexity reduction via tailored viscoelastic damping co-design. In AAS G&C Conference, 2018, Breckenridge, CO, USA.
7. Corman R E, Rao L, Bharadwaj N A, Allison J T, and Ewoldt R H. Setting material function design targets for linear viscoelastic materials and structures. Journal of Mechanical Design, 2016, 138(5): p. 051402.
8. Vedant and Allison J T. Pseudo-Rigid Body Dynamic Modeling of Compliant Members for Design. In ASME IDETC/CIE, 2019, Anaheim, CA, USA. to appear.
9. Bird R B, Armstrong R C, and Hassagar O. Dynamics of Polymeric Liquids: Volume 1 Fluid Mechanics. 2nd ed. New York: Wiley, 1987.